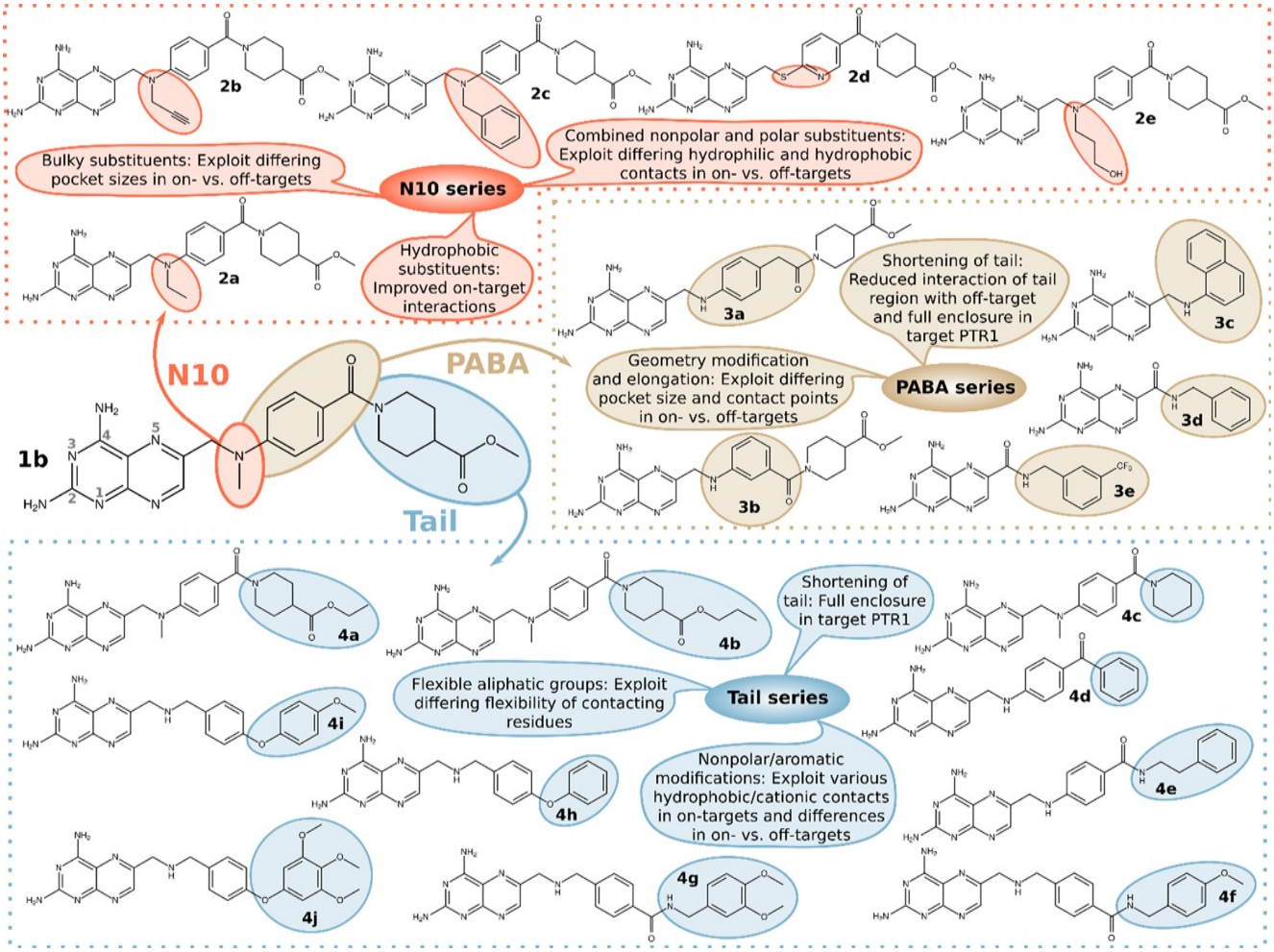

Figure 6. Overview of the modifications in the N10, PABA, and Tail modules explored in the designed compound series with respect to the reference compound **1b**. Synthesized members of each designed series are shown in the framed boxes along with the key objectives addressed with the respective modifications. See text for details.

Scheme 1. Synthesis of Derivatives of Compound 29[a]

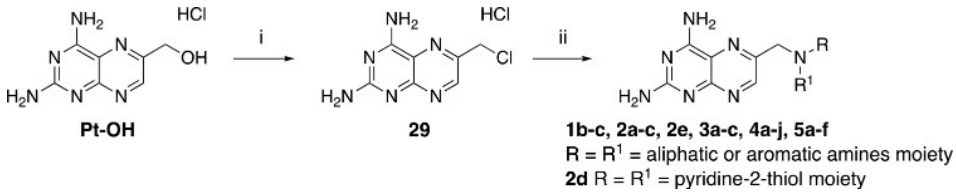

[a]Reagents and conditions: (i) $SOCl_2$, reflux, 12 h, 70% yield; (ii) **29** (1.2 equiv), corresponding amine derivative (1 equiv), K_2CO_3 (3 equiv), KI (0.1 equiv), DMA, 60°C, 20′−30′ MW.

distinguishing on- and off-targets and the distinct surroundings of the tail in PTR1 vs DHFR.

Synthesis of Pteridine Derivatives with High Yield. A total of 26 new 2,4-diaminopteridine derivatives and the reference compounds **1b** and **1c** were (re)synthesized as reported in Schemes 1−8. We applied our methodology for an improved reaction yield of the chemical pteroid step to provide a key intermediate for most of the designed compounds.[33] Displacement of the chloride of 6-(chloromethyl)pteridine-2,4-diamine hydrochloride (**29**, Scheme 1) by the appropriate substituted anilines and aliphatic amino derivatives was carried out in *N*,*N*-dimethylacetamide (DMA) at 60 °C microwave (MW) to provide **1b**,**c**, **2a**−**e**, **3a**−**c**, **4a**−**j**, and **5a**−**f** in high yields of 70−90% with reduced reaction time (Schemes 2−7).[33]

The PABA amine functionalization was achieved by selective alkylation of primary amines to secondary amines using nitriles as alkylating reagents with Pd/C for intermediates **32** and **33**.[34,35] Conventional alkylation of the latter with propargyl bromide or (bromomethyl)benzene resulted in derivatives **34** and **35**, respectively (Scheme 2).

The reductive alkylation of amines using nitriles was also used to obtain **51** and **74** in Schemes 3 and 7. The isonipecotic acid derivatization was achieved via Fischer esterification using the reagent solvents propanol (**37**) and EtOH (**38**), respectively;

https://doi.org/10.1021/acs.jmedchem.2c00232
J. Med. Chem. 2022, 65, 9011−9033

Scheme 2. Synthesis of Compounds 1b,c, 2a−c, 2e, 4a−c, and 5c, and Intermediates 32−35, 37, 38, and 40−49[a]

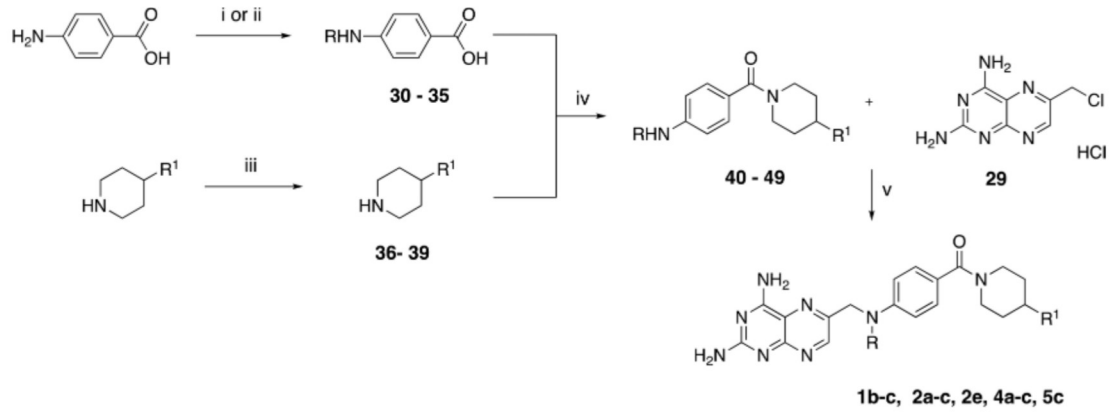

	R=	R¹=
30	CH_3	–
31	H	–
32	CH_2CH_3	–
33	$CH_2CH_2CH_2OH$	–
34	CH_2CCH	–
35	$CH_2C_6H_5$	–
36	–	$COOCH_3$
37	–	$COOCH_2CH_2CH_3$
38	–	$COOCH_2CH_3$
39	–	H

		R=	R¹=
40	1b	CH_3	$COOCH_3$
41	1c	H	$COOCH_3$
42	2a	CH_2CH_3	$COOCH_3$
43	2e	$CH_2CH_2CH_2OH$	$COOCH_3$
44	2b	CH_2CCH	$COOCH_3$
45	4b	CH_3	$COOCH_2CH_2CH_3$
46	4a	CH_3	$COOCH_2CH_3$
47	5c	CH_2CH_3	$COOCH_2CH_3$
48	2c	$CH_2C_6H_5$	$COOCH_3$
49	4c	CH_3	H

[a]Reagents and conditions: compounds **30**, **31**, **36**, and **39** were purchased from Sigma; (i) acetonitrile or 3-hydroxypropanenitrile, 10% Pd/C, NH_4OAc (1 equiv), CH_3OH, H_2, rt, 24−36 h (**32**, **33**); (ii) alkyl halide (propargyl bromide, (bromomethyl)benzene) (0.5 equiv), K_2CO_3 (2 equiv), DMF dry, rt, 24 h (**34**, **35**); (iii) $SOCl_2$ (4 equiv), propanol (for **37**), EtOH (for **38**), reflux, 7−12 h (89 and 96% yield); (iv) EDC·HCl (1.1 equiv), HOBt (0.1 equiv), TEA (2−3 equiv), DMF, rt, overnight (**40**−**49**); (v) **29** (1.2 equiv), corresponding amine derivative (1 equiv), K_2CO_3 (3 equiv), KI (0.1 equiv), DMA, 20′ MW (**1b,c**, **2a−c**, **2e**, **4a−c**, **5c**).

Scheme 3. Synthesis of Compounds 3a and 5a,b[a]

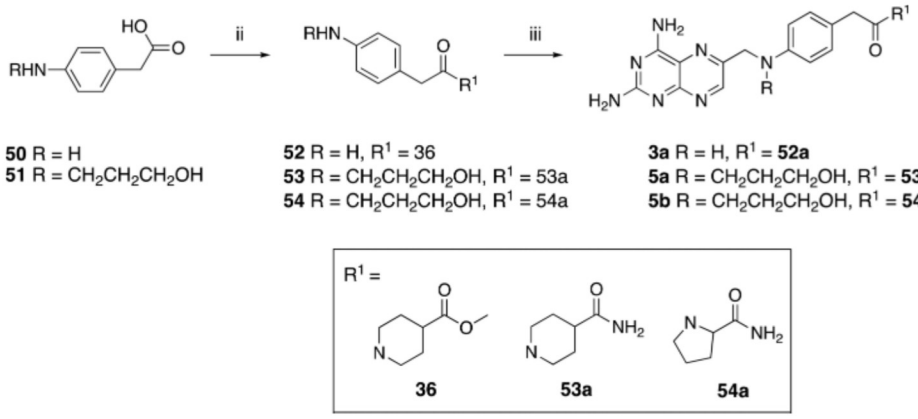

[a]Reagents and conditions: (i) 3-hydroxypropanenitrile, 10% Pd/C, NH_4OAc (1 equiv), CH_3OH, H_2, rt, 24 h (**51**); (ii) EDC·HCl (1.1 equiv), HOBt (0.1 equiv), TEA (2−3 equiv), DMF, rt, overnight (**52**−**54**); (iii) **29** (1.2 equiv), corresponding amine derivative (1 equiv), K_2CO_3 (3 equiv), KI (0.1 equiv), DMA, 20′ MW (**3a**, **5a,b**).

methyl isonipecotate (**36**) and piperidine (**39**) were purchased from Sigma (Scheme 2).

The intermediate acid derivatives **30**−**35** and **d** and **e** were condensed to amides through a coupling reaction with the respective amines **36**−**39** and **g** using EDC·HCl in dimethylformamide (DMF) as the coupling agent to provide the intermediate products **40**−**49**, **71**, **72**, and **75**, which were then made to react with **29** to obtain the final compounds (**1b,c**, **2a−d**, **3b**, **4a−c**, **4e**, **5c**; Schemes 2, 6, 7).

Using the same method, we synthesized the elongated compounds **3a**, **4f−g**, and **5a,b**, characterized by a carbon spacer in the PABA moiety (Schemes 3 and 4).

To obtain **4f,g** (Scheme 4), an additional protection step reaction to guide selective amide functionalization was

https://doi.org/10.1021/acs.jmedchem.2c00232
J. Med. Chem. 2022, 65, 9011−9033

Scheme 4. Synthesis of Compounds 4f,g[a]

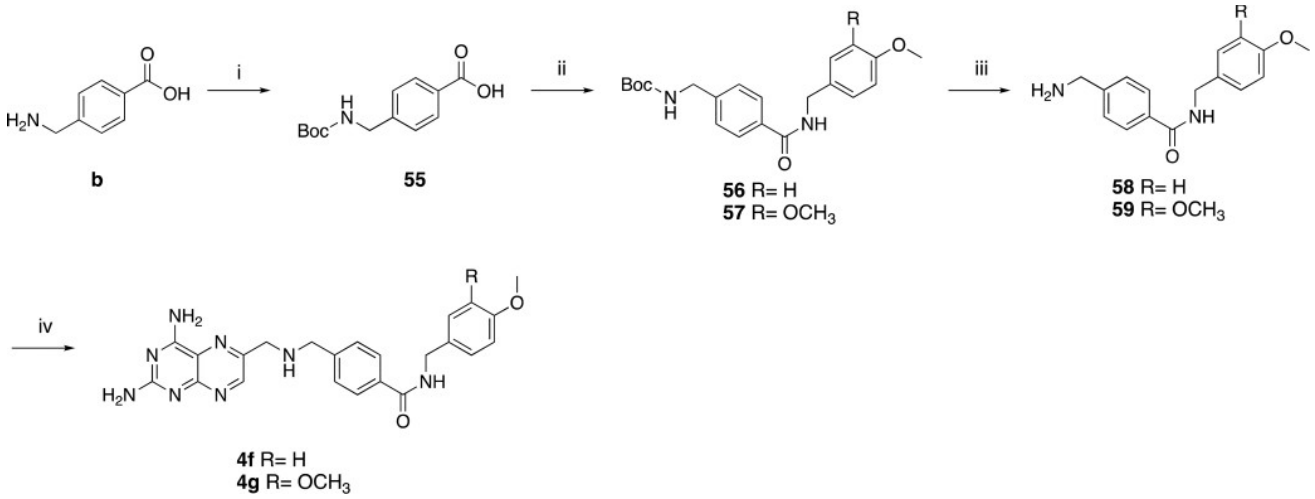

[a]Reagents and conditions: (i) di-*tert*-butyl pyrocarbonate (1.05 equiv), dioxane/H_2O/1 N NaOH 1/1/1 V/V/V, rt, 6 h (**55**); (ii) EDC·HCl (1.1 equiv), HOBt (0.1 equiv), TEA (2−3 equiv), DMF, rt, overnight (**56** and **57**); (iii) TFA, DCM, rt (**58** and **59**); (iv) **29** (1.2 equiv), corresponding amine derivative (1 equiv), K_2CO_3 (3 equiv), KI (0.1 equiv), DMA, 20′ MW (**4f,g**).

Scheme 5. Synthesis of Compounds 4h−j and 5e,f[a]

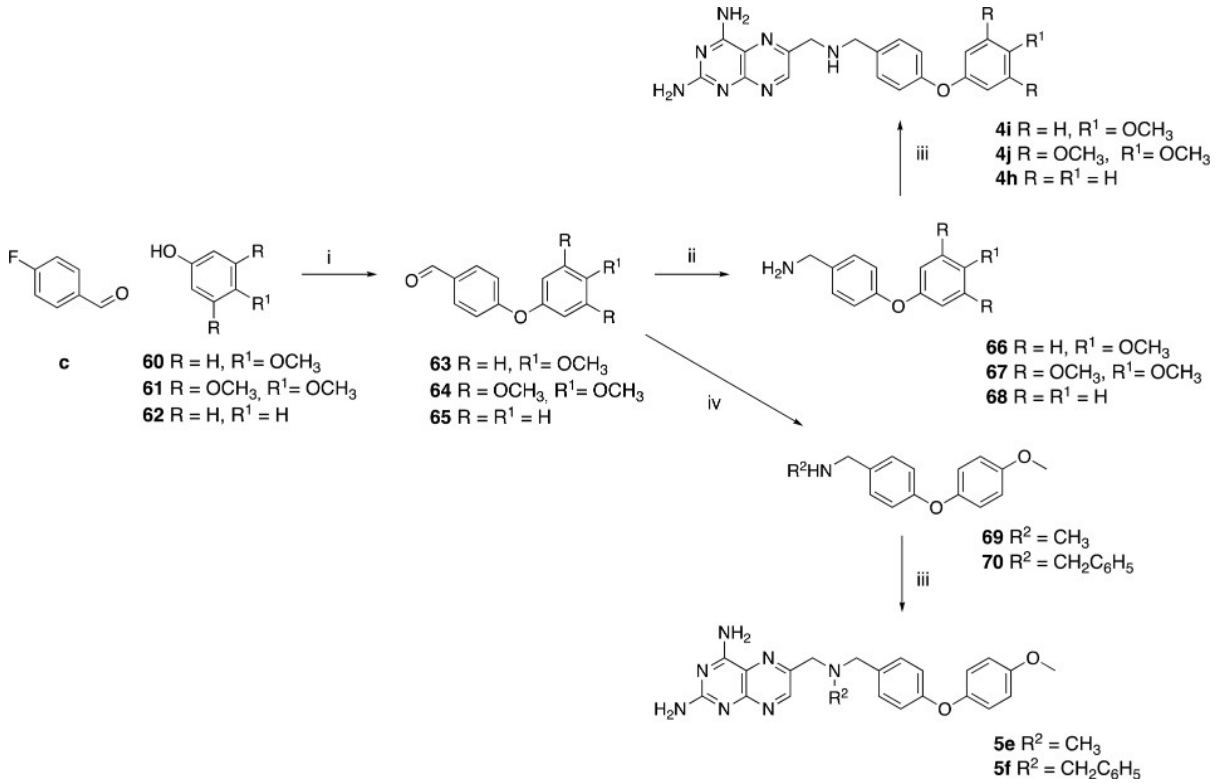

[a]Reagents and conditions: (i) K_2CO_3 (3 equiv), DMF, reflux, 16−18 h (**63−65**); (ii) NH_2OH·HCl (1.2 equiv), EtOH, rt, >1 h followed by Zn dust (2.5 equiv) in 12 M HCl (4 equiv), rt, 15′ (**66−68**); (iii) **29** (1.2 equiv), corresponding amine derivative (1 equiv), K_2CO_3 (3 equiv), KI (0.1 equiv), DMA, 20′ MW (**4h−j**, **5e,f**); (iv) methylamine (for **69**) or benzylamine (for **70**), EtOH dry, 60°C, 3 h, then $NaBH_4$ (1.5 equiv), rt, 2 h.

necessary. The selectivity was achieved via Boc protection in the first step of the reaction of **b** to obtain **55**, which was then coupled with the respective aliphatic amine to give **56** and **57**. The target amines were finally obtained by a deprotection step carried out in 30−40% trifluoroacetic acid/dichloromethane (TFA/DCM) in quantitative yield.

The phenoxyphenyl−methanamine derivative intermediates (Scheme 5) were synthesized starting from 4-fluorobenzaldehyde and the respective phenol derivates **60−62** by an S_NAr reaction. Subsequently, the primary amines **66−68**,[36] or functionalized amines **69** and **70** (obtained via a one-pot reductive step), were reacted with **29** to obtain **4h−j** and **5e,f**.

https://doi.org/10.1021/acs.jmedchem.2c00232
J. Med. Chem. 2022, 65, 9011−9033

Scheme 6. Synthesis of Compounds 3b and 2d[a]

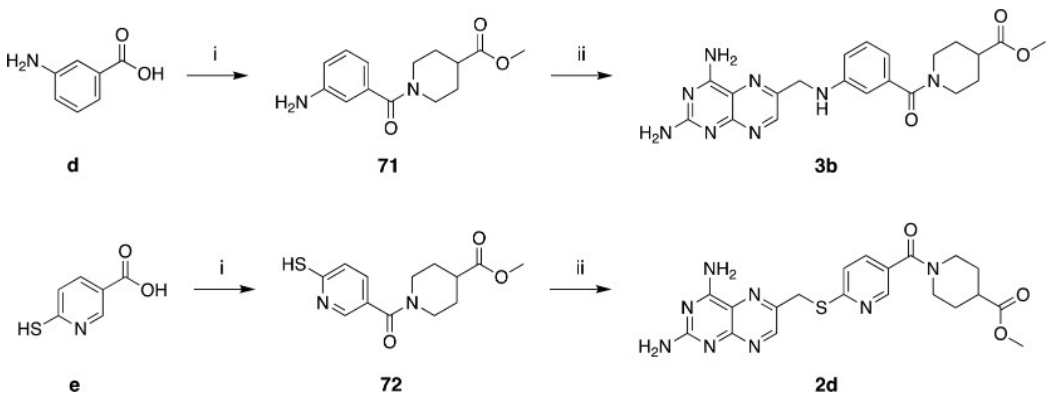

[a]Reagents and conditions: (i) EDC·HCl (1.1 equiv), HOBt (0.1 equiv), TEA (2−3 equiv), DMF, rt, overnight (**71** and **72**); (ii) **29** (1.2 equiv), corresponding amine derivative (1 equiv), K_2CO_3 (3 equiv), KI (0.1 equiv), DMA, 20′ MW (**3b**, **2d**).

Scheme 7. Synthesis of Compounds 3c, 4d,e, and 5d[a]

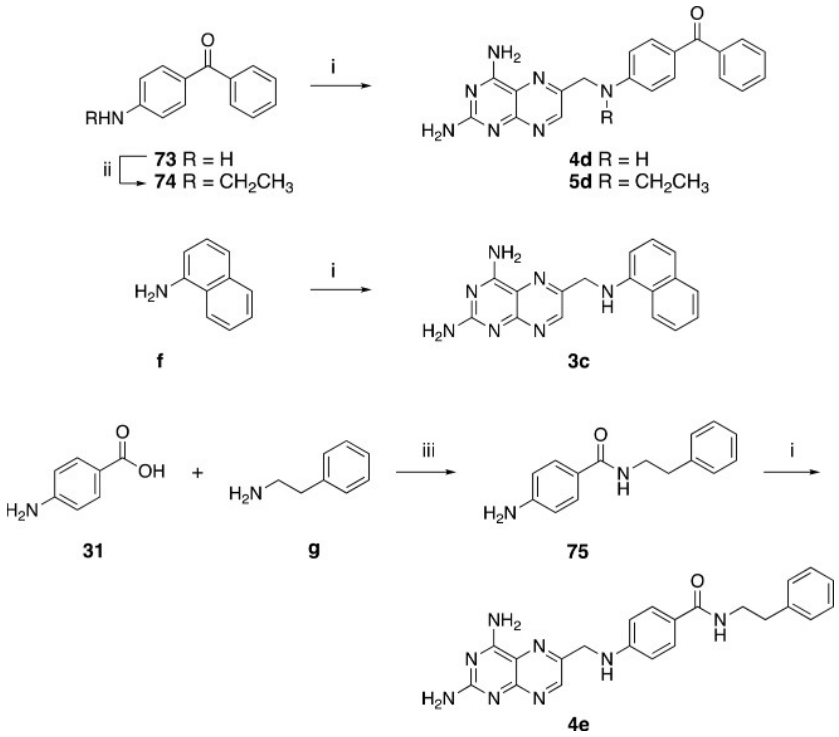

[a]Reagents and conditions: (i) **29** (1.2 equiv), corresponding amine derivative (1 equiv), K_2CO_3 (3 equiv), KI (0.1 equiv), DMA, 30′ MW (**3c**, **4d,e**, and **5d**); (ii) acetonitrile, 10% Pd/C, NH_4OAc (1 equiv), CH_3OH, H_2, rt, 24−36 h (**74**); (iii) EDC·HCl (1.1 equiv), HOBt (0.1 equiv), TEA (2−3 equiv), DMF, rt, overnight (**75**).

Scheme 8. Synthesis of Compounds 3d,e[a]

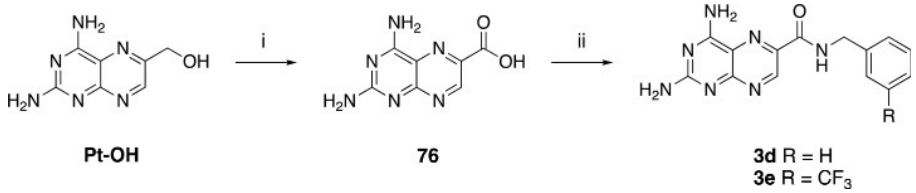

[a]Reagents and conditions: (i) $KMnO_4$, acetone/0.5 M phosphate buffer at pH 7 (1:1 V/V); (ii) EDC·HCl (1.1 equiv), HOBt (0.1 equiv), TEA (2−3 equiv), DMF, rt, overnight.

https://doi.org/10.1021/acs.jmedchem.2c00232
J. Med. Chem. 2022, 65, 9011−9033

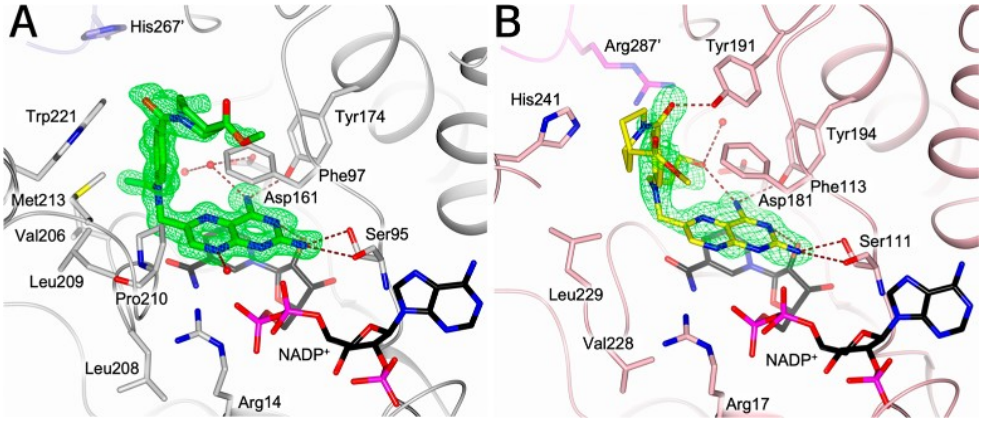

Figure 7. Views of the binding sites of crystal structures of complexes of pteridine-based inhibitors in *Tb*PTR1 and *Lm*PTR1 determined in this work, which confirm the predicted MTX-like binding modes. (A) **2a** (green carbons) in *Tb*PTR1 (gray cartoon, His267′ from the neighboring subunit in lavender) and (B) **2e** (yellow carbons) in *Lm*PTR1 (pink cartoon, Arg287′ from the neighboring subunit in magenta). Water molecules are shown as red spheres, and the inhibitors are surrounded by the omit map (green wire) contoured at the 2.5 σ level. Interacting residues and the NADPH/$NADP^+$ cofactor are shown in sticks (carbons colored according to protein and black, respectively). Hydrogen bonds are represented by brown dashed lines.

Compounds **3c**, **4d**, and **5d**, with a higher steric hindrance, were obtained with a slightly increased reaction time in a good yield. Finally, to obtain **3d**,**e**, it was necessary to first perform an oxidation reaction. Treatment of Pt−OH in acetone/0.5 M phosphate buffer at pH 7 (1:1 v/v) with $KMnO_4$ gave the oxidized analogue **76**, which was subsequently coupled with the selected aliphatic amine to obtain the desired amides (Scheme 8).

Crystal Structures for the PTR1 Targets Confirm the Predicted Interactions and That the Pteridine Derivatives Adopt a Methotrexate-Inhibitor-Like Orientation. The structures of *Tb*PTR1 with two new pteridines, **2a** and **2e**, and that of *Lm*PTR1 with **2e**, were determined to 1.20, 1.11, and 2.10 Å resolution, respectively (see Tables S2 and S3). The structures contain functional enzyme tetramers in the crystallographic asymmetric unit with a similar structure to those previously determined.[37,38] In all complexes, the compounds adopt MTX-like binding modes (Figure 7A,B).

In line with the docking predictions, the overall structure of the *Tb*PTR1 complexes resembles the complex with **1b** (compare Figure 7A with 3C). In agreement with the design objective, the *N*-ethyl moiety of **2a** was found to form van der Waals interactions with Val206 and Trp221 on the hydrophobic side of the pocket (Figure 7A). The bulkier N-propylhydroxyl moiety of **2e** forms direct and water-mediated hydrogen bonds with Asp161 and receives an intramolecular hydrogen bond from the amine in position 4 on the pteridine system (Figure S2C). The structure of *Lm*PTR1 in complex with **2e** (Figure 7B) closely resembles that observed in *Tb*PTR1, except for the terminal piperidine moiety (Figure S2C,D). The latter moiety is highly flexible—a possible orientation is reported in the crystal structure, but further orientations cannot be excluded.

Designed Pteridine Derivatives Have Improved Target and Off-Target Enzyme Inhibitory Activities. The measured inhibitory activities of compounds **2a**−**e**, **3a**−**e**, and **4a**−**j** against the targets *Tb*PTR1, *Tb*DHFR, *Lm*PTR1, and *Lm*DHFR and the off-targets hDHFR and hTS are given in Figure 8 and Table S1. All inhibitory activities are reported as IC_{50} values, which are commonly used to characterize and rank compounds when screening for enzyme inhibition in drug discovery projects.[39] Overall, the inhibitory activities against the PTR1 targets for the designed compounds are improved, as are PTR1 vs off-target selectivities. Indeed, for a small number of compounds (**2c**, **2d**, **4c**, **4d**, **4e**, **5c**, and **5d**), the IC_{50} values for inhibition were determined to be either 1 nM or less than 0.1 nM against *Tb*PTR1. As the *Tb*PTR1 assay makes use of low nanomolar concentrations of enzyme, for these very potent compounds, the tight binding limit was approached, and therefore, accurate values of the IC_{50} values could not be determined.[40] Representative dose−response curves are shown in the Supporting Information, showing that only part of the response range could be measured for these compounds for which the IC_{50} value could also be rather sensitive to any possible errors in dilution or determination of inhibitor or enzyme active site concentration.

N10 Modifications Yield Improved PTR1 Inhibitors with Similar Selectivity Trends for Parasite DHFRs. The N10-modified compounds (**2a**−**e**; Figure 6) are improved PTR1 inhibitors in comparison to **1b**, except for **2a** (**1b** IC_{50} *Tb*PTR1 50 nM, *Lm*PTR1 1 μM; N10 series IC_{50} *Tb*PTR1 < 0.1−90 nM; *Lm*PTR1 0.02−13.3 μM; Figure 8). **2c** is the best in the series with IC_{50} < 0.1 nM against *Tb*PTR1 and an IC_{50} of 20 nM against *Lm*PTR1.

All compounds are roughly similar to **1b** in parasite DHFR inhibition (**1b** IC_{50} *Tb*DHFR and *Lm*DHFR 0.3 μM; N10 series IC_{50} *Tb*DHFR 0.4−2.4 μM, *Lm*DHFR 0.5−9.4 μM), and selectivities over hDHFR range from 7- to 66-fold for *Tb*DHFR and 9- to 110-fold for *Lm*DHFR, which are somewhat lower than for **1b** (SI *Tb*DHFR/hDHFR = 164 and *Lm*DHFR/hDHFR = 167). Thus, mainly PTR1 inhibition benefits from the selected N10 modifications.

PABA Modifications Lead to Strong Variations in the Target Inhibition Profile. The modifications of the PABA moiety in the PABA series (compounds **3a**−**e**; Figure 6) distinctly affect the inhibitory activities against the targets. Smaller compounds with well-enclosed binding poses show varying improvements in inhibitory activity for different PTR1 variants: **3c**, in contrast to most of the studied pteridines, is equipotent toward *Lm*PTR1 and *Tb*PTR1 (IC_{50} 10 nM). This notable improvement of *Lm*PTR1 activity is in line with its predicted good steric fit to the *Lm*PTR1 binding pocket shape (compare Figures 4C and 5C). Full enclosure and stabilizing interactions with hydrophobic residues lining the pocket entrance likewise probably contribute to an around 10-fold

https://doi.org/10.1021/acs.jmedchem.2c00232
J. Med. Chem. 2022, 65, 9011−9033

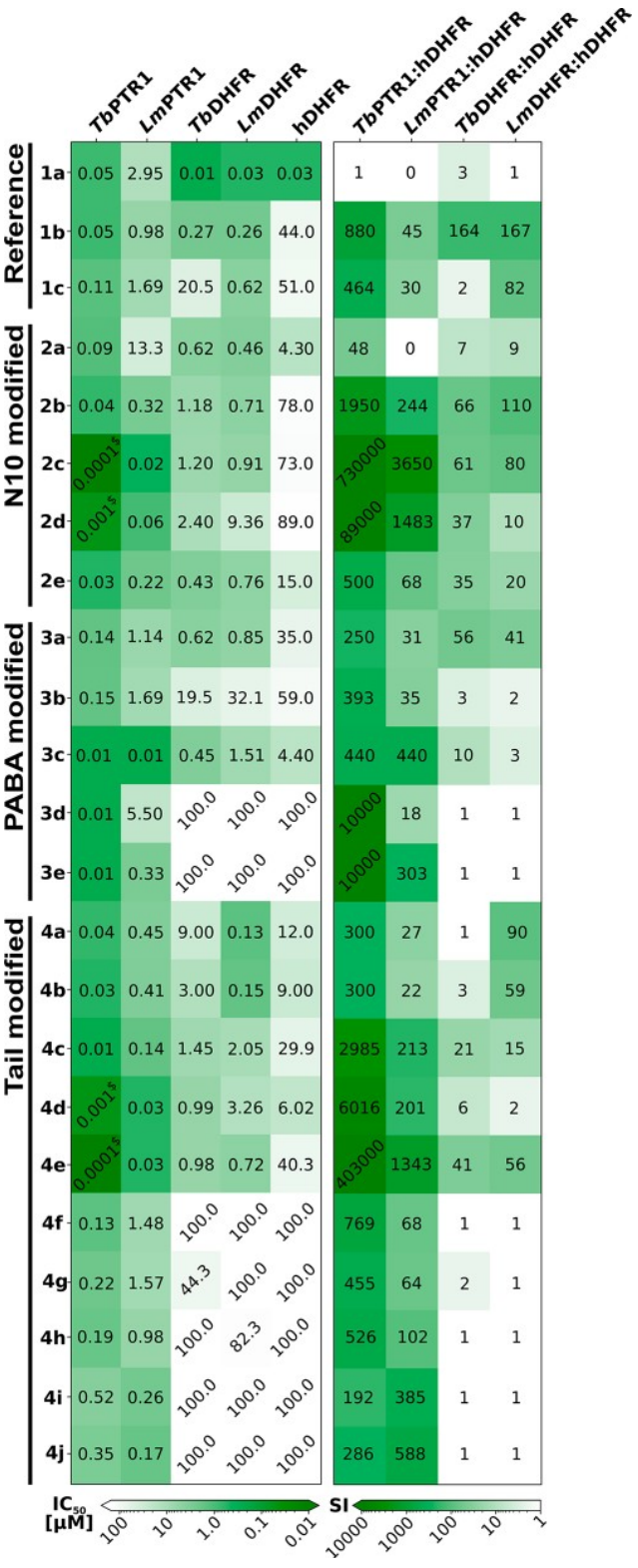

Figure 8. Inhibitory activities (IC_{50} values, left) and selectivities (selectivity indices (SI), right) of compounds of the designed N10-, PABA-, and Tail-modified series and selected reference compounds against the targets *Tb*PTR1, *Lm*PTR1, *Tb*DHFR, and *Lm*DHFR and the off-target hDHFR. All values, as well as data for hTS, are reported in Table S1. Greener boxes show higher inhibition and selectivity. $ indicates that a precise activity value could not be determined as the tight binding limit was approached.

higher potency of **3d** and **3e** against *Tb*PTR1 than the most similar reference compound **1c** (lacking an N10 substitution) (IC_{50} **3d**, **3e**: 10 nM; **1c**: 110 nM).

Whereas **3d** and **3e** do not show inhibitory activity against the parasite DHFR targets, **3c** shows similar activity against *Lm*DHFR to **1c** (IC_{50} 1.5 and 0.6 μM, respectively) and displays higher activities against both *Tb*DHFR (IC_{50} **1c**: 20.5 μM; **3c**: 0.5 μM) and hDHFR (IC_{50} **1c**: 51 μM; **3c**: 4 μM). A one-carbon spacer to shift the position of the PABA carbonyl in **3a** with respect to **1c** improves inhibition of *Tb*DHFR (IC_{50} 0.6 μM) while not significantly affecting inhibition of *Lm*DHFR and hDHFR. Thus, **3a** is more selective against TbDHFR than the reference **1c** (SI: 56 vs 2).

Taken together, alterations to the PABA moiety, due to its central location in the compound scaffold, different pocket sizes, and surrounding residue patterns in targets (Figure 4A) display highly variable effects on the activity profiles.

Alterations in Tail Geometry Boost PTR1 Inhibition but Can Reduce DHFR Inhibition. In the Tail-modified series (compounds **4a**−**j**; Figure 6), hydrophobic and aromatic residues lining the pocket entrance region of PTR1 were exploited by either tail elongation or shortening. The interactions of these residues with the flexible aromatic tail of **4e** (see Figure 5E) likely contribute to the boost of the IC_{50} against *Tb*PTR1 to the subnanomolar range and to 30 nM against *Lm*PTR1; these are 1000-fold and 57-fold improvements, respectively, in PTR1-inhibitory potencies compared to reference compound **1c**. The shortened tails of **4c** (unsubstituted piperidine) and **4d** (benzene) are stabilized by the same residues and likely benefit from a better enclosure in the PTR1 pocket. Both compounds show improved *Tb*PTR1 and *Lm*PTR1 inhibition compared to **1b** (IC_{50} *Tb*PTR1 **4c**: 10 nM, **4d**: 1 nM vs **1b**: 50 nM; *Lm*PTR1 **4c**: 0.1 μM, **4d**: 0.03 μM vs **1b**: 1.0 μM).

However, shortening of the tail diminishes the inhibition of parasite DHFR, whereas it either does not affect or increases inhibition of the off-target hDHFR. Revisiting the docking predictions provides a possible explanation for this: The piperidine/benzene groups in the tails of **4c** and **4d** can form more extended hydrophobic interactions with Phe31 of hDHFR than with the corresponding methionine in the parasite DHFR variants (Figure 9). In the parasite protein, moreover, Asn64 in the pocket entrance of hDHFR is replaced by phenylalanine, which, upon interaction with the compound tail, becomes solvent-exposed.

Pocket size and interaction pattern differences between *Lm*DHFR and other DHFR variants, as also discussed for the PABA series, also affect the Tail-modified compounds: for instance, **4d** is more active against both *Tb*DHFR and hDHFR than **1c** (IC_{50} *Tb*DHFR 1 vs 21 μM, hDHFR 6 vs 51 μM), while both compounds show similar activity for *Lm*DHFR.

Summary of the Compound Activity Profiles for the N10, PABA, and Tail-Modified Series. Taken together, most of the new pteridine derivatives display 1−2-fold greater inhibition of *Tb*PTR1 than *Lm*PTR1 and are more or equally active against PTR1 than the reference compound **1b**. The nanomolar to subnanomolar PTR1 inhibitors show improved selectivity for PTR1 over the off-target hDHFR by up to about 3 orders of magnitude (**2c**, **4e**: *Tb*PTR1 IC_{50} < 0.1 nM; SI > 400 000) (Figure 8). The IC_{50} against hDHFR is typically greater than 100 μM, whereas inhibitory activities against *Tb*DHFR and *Lm*DHFR are higher. For parasite DHFR, the compounds with the best inhibitory activities have similar IC_{50}

https://doi.org/10.1021/acs.jmedchem.2c00232
J. Med. Chem. 2022, 65, 9011−9033

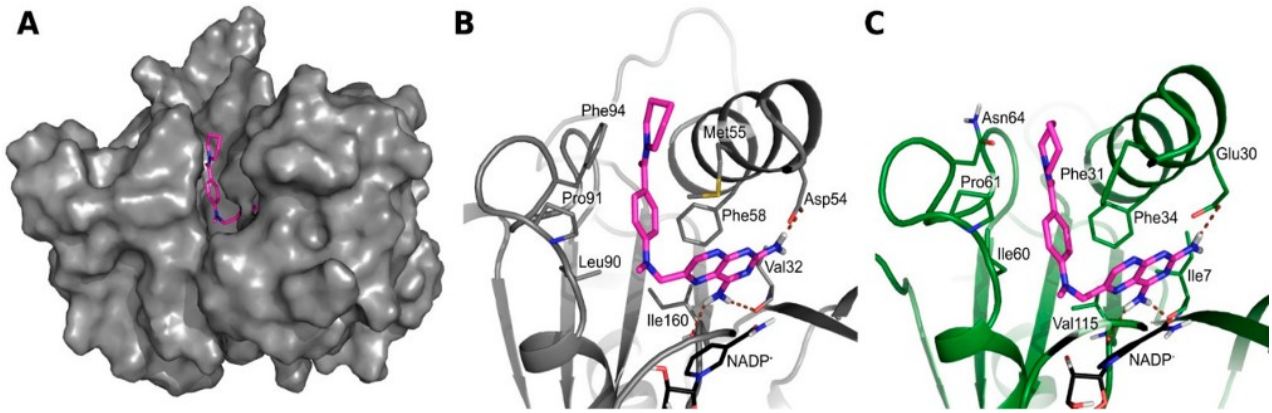

Figure 9. Docking poses for compound **4c** from the Tail series (magenta carbons) in (A,B) *Tb*DHFR and (C) hDHFR, showing differences in exposure and interactions of the PABA and Tail moieties in the two DHFRs. (A) *Tb*DHFR pocket accommodates **4c** with its tail enclosed by surrounding residues. hDHFR has a similar shape. *Tb*DHFR is shown in a gray surface representation. (B,C) Views of the binding sites of *Tb*DHFR and hDHFR, which are shown in cartoon representation in gray and green, respectively. Important interacting residues and the NADPH/$NADP^+$ cofactor (black carbons) are shown as sticks. Hydrogen bonds are indicated by brown dotted lines. While the orientations of **4c** are rather similar in both DHFR variants, the tail moiety is more solvent-exposed in *Tb*DHFR: the PABA benzene and piperidine of **4c** compete for interactions with Phe94 of *Tb*DHFR, which thereby becomes exposed to the solvent. In hDHFR, the corresponding exposed residue is the polar Asn64, and the tail of **4c** can interact with Phe31 deeper in the pocket, rendering the mode of binding more favorable in hDHFR. The results are presented for N1-deprotonated compounds, but similar observations were made with N1-protonated compounds (Figure S6).

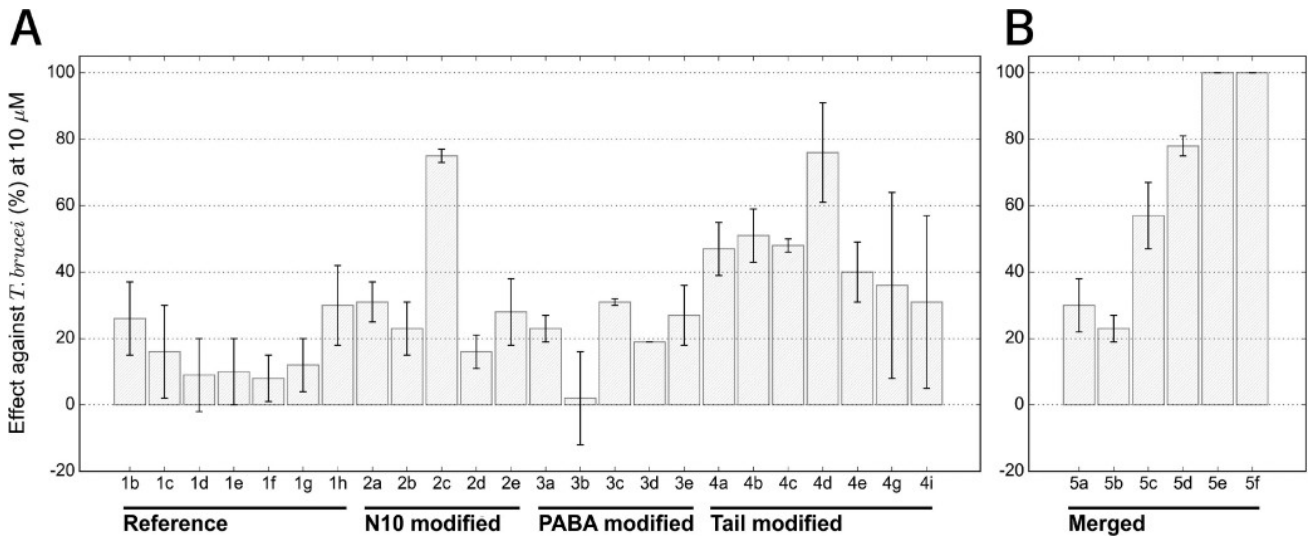

Figure 10. Antiparasitic activity expressed as percentage of inhibition against *T. brucei brucei* for reference compounds and members of the N10-, PABA-, and Tail-modified series (A) and the selected representatives of the merged *in silico* library (B). The average of at least three independent determinations is shown with the standard deviation. The inactive compounds in the Tail-modified series, **4f**, **4h**, and **4j** were omitted. Activities can be found in Table S7.

values to **1b** (e.g., *Lm*DHFR IC_{50} **4a**: 0.13 μM, **4b**: 0.15 μM, and **1b**: 0.26 μM). Thus, the newly designed compounds show improved target inhibitory profiles, particularly for the PTR1 targets, and overall good selectivity for the parasitic proteins.

Inhibitory Activity against *T. brucei* Is Related to the Hydrophobicity of the Compounds. Following the assessment of the improvement on the target inhibition level, we next determined the antiparasitic effect on *T. brucei brucei* Lister 427 bloodstream forms and *L. infantum* intramacrophage amastigotes (Figure 10A and Table S7). The *Lm*PTR1 and *Lm*DHFR proteins are highly similar to the corresponding *L. infantum* proteins (91 and 96% sequence identity, respectively), but in spite of the improved effect on both target proteins, the designed pteridines are mostly inactive against *L. infantum*. In contrast, the compounds show activity against *T. brucei.*

The multiple correlation coefficient between the *Tb*PTR1 and *Tb*DHFR IC_{50} values and the *T. brucei* bloodstream form inhibition is R = 0.35 (eq 3, SI), indicating that the levels of target enzyme inhibition are, for the current compounds, only weakly correlated with the exhibited antiparasitic effect when assuming a linear correlation. PTR1 inhibition alone shows a Pearson correlation R = 0.34 with *T. brucei* inhibition, whereas R is only 0.24 for DHFR inhibition, possibly because all studied compounds are much stronger inhibitors of PTR1 than DHFR. The low correlation for DHFR inhibition might also arise because of the competition from the high folate concentration in the medium in the parasite assays.

Another reason for the low correlations between parasite and target protein inhibition could be transport issues. For example, the charged compound tail and possible polyglutamylation of

https://doi.org/10.1021/acs.jmedchem.2c00232
J. Med. Chem. 2022, 65, 9011−9033

Table 1. Descriptors with Significant Correlations with the Observed Inhibitory Effect on *T. brucei* for the Reference Compounds and Pteridines of the N10-, PABA-, and Tail-Modified Series Calculated with QikProp[43a]

predicted property	QPlogKp	QPlogPo/w	QPlogKhsa	cohesive index	CIQPlogS
R	0.55	0.49	0.47	−0.41	−0.54
R^2	0.30	0.24	0.22	0.17	0.29
P-value	0.003	0.01	0.01	0.04	0.004
resampling recovery rate (%)	100	96	96	56	96
optimization direction	↑	↑	↑	↓	↓
covered range	−6.62 − −3.60	−1.02−2.92	−0.85−0.35	0.02−0.04	−6.71 − −3.19
recommended range	−8.00 − −1.00	−2.00−6.50	−1.50−1.50	0.00−0.05	−6.50−0.50

[a]QPlogKp: Predicted skin permeability, log K_p; QPlogPo/w: Predicted octanol/water partition coefficient. QPlogKhsa: Prediction of binding to human serum albumin. Cohesive index: Index of cohesive interaction in solids, (number of hydrogen bond acceptors × number of hydrogen bond donors × 0.5/surface area);[44] CIQPlogS: Conformation-independent predicted aqueous solubility, log S with S in mol dm^{-3} being the concentration of the solute in a saturated solution that is in equilibrium with the crystalline solid. R (Pearson correlation) and R^2 were calculated using the percentage of inhibition of the *T. brucei brucei* Lister 427 bloodstream form at a 10 μM compound concentration as defined in the SI. Only descriptors with at least a Pearson correlation/anticorrelation of 0.40/−0.40 and two-tailed P-values lower than the chosen significance level α of 0.05 are reported. The covered range lists property values obtained for the studied compounds, while the recommended range lists values the properties take for typical drug-like molecules. The resampling recovery rate indicates in how many cases (expressed as percentage) the same property was identified when leaving a single compound out of the data set. The optimization direction indicates whether higher or lower values would putatively lead to improved anti-parasitic effects.

the parent MTX (**1a**) have previously been suggested to influence compound transport.[41,42] All the newly designed pteridines lack the glutamate tail, which may affect their *in vivo* activities, but there might be other structural or physicochemical features that render them more or less active against parasites despite similar target inhibition. For example, for *T. brucei*, we noticed that while **2c** and **4e** have similar effects on the targets *Tb*PTR1 (0.1 nM) and *Tb*DHFR (approximately 1 μM), they differ notably in their inhibitory effect on the parasite bloodstream forms (75 vs 40%).

Therefore, we investigated the correlations of physicochemical properties and ADMET predictors with the measured effect on *T. brucei*; see Table 1. Our aim was to identify which properties were indicative of a better antiparasitic effect, possibly related to better uptake. Overall, only weak correlations of the individual properties with *T. brucei* inhibition were observed (Pearson R: 0.47−0.55 and −0.41 − −0.54; computed as defined in the SI). The strongest correlation was found for the predicted skin permeability, QPlogKp, as a descriptor linked to lipophilicity, (R: 0.55). The logPo/w and the binding to human serum albumin had slightly weaker correlations with the antiparasitic effect (R: 0.49 and 0.47, respectively). For these properties, an increase in the value corresponds with higher anti-*T. brucei* activity. In contrast, some properties showed anticorrelation, for instance, the aqueous solubility and the cohesive index[44] (R: −0.54 and −0.41, respectively). Taken together, the data indicate an improved antiparasitic effect with increased lipophilicity of the studied compounds.

Combined Modifications Yield Pteridines with Both Improved Target Inhibition and Improved Antiparasitic Activity. To explore further derivatives of the studied pteridines, we next designed a merged compound library as follows. The pteridine core scaffold was retained, and the studied compounds were decomposed into fragments of their N10, PABA, and Tail regions and recombined *in silico* in all possible combinations to yield 2014 derivatives (see SI for details). These derivatives were evaluated in docking studies against targets and off-targets and additionally prioritized by the physicochemical marker properties that showed correlations with the anti-*T. brucei* effect (Figure S9). Of the remaining 600 candidates, 6 were selected by expert opinion as representative compounds for synthesis and experimental evaluation (**5a**−**5f**, Figure 11).

Two compounds, **5a** and **5b**, were chosen for their favorable interaction patterns and scores predicted by docking simulations. **5a** combines the N10 hydroxypropyl fragment of **2e**, benzyl in place of the PABA phenyl of **3a**, the tail amide of reference compound **1g**, and, for **5b**, in addition, the tail pyrrolidine of ref **1h**, which replaces the tail piperidine. The activities and predicted interactions in all parasite targets are most similar to **2e**, suggesting the key importance of the hydroxy-propyl substituent to N10 for the target inhibition. Notably, while **5a** is poorly selective for *Tb*DHFR (2-fold) and modestly selective for *Lm*DHFR (31-fold), **5b** is inactive against hDHFR, resulting in SI values of 169 and 113 for *Tb*DHFR and *Lm*DHFR, respectively. Moreover, **5b** has SI values over hDHFR of about 25 000 for *Tb*PTR1 and 588 for *Lm*PTR1. However, in contrast to most compounds, **5b** displays a weak inhibition of hTS (IC_{50} 29 μM, Table S1).

Four additional compounds (**5c**−**5f**, Figure 11) were prioritized based on the physicochemical marker properties. Compound **5c** combines fragments of ethyl modification to N10 of **2a** and the tail ethyl ester of **4a**. Due mainly to the tail ester, this modification improves the inhibition for both *Tb*PTR1 (IC_{50} 1 nM) and *Lm*PTR1 (IC_{50} 0.1 μM). The activity against *Tb*DHFR is similar to that of the N10-modified parent **2a**, whereas *Lm*DHFR and hDHFR inhibition are again influenced by the tail modification (IC_{50} *Lm*DHFR **5c**: 0.2 μM, **4a**: 0.1 μM; hDHFR **5c**: 13 μM, **4a**: 12 μM). Compound **5d** merges the ethyl N10 fragment of **2a** with the unsubstituted benzene of **4d**. In *Tb*PTR1, this boosts the nanomolar IC_{50} of **4d** to the subnanomolar range, while the activity toward *Lm*PTR1 remains similar to **4d**. This profile can be related to the N10 ethyl, which seems disfavored in *Lm*PTR1 as judged by the modest inhibition of the parent **2a** (IC_{50} 13.3 μM).

Compounds **5e** and **5f** combine the ethylphenyl(4-methoxyphenyl) ether scaffold of **4i** with the benzyl and methyl N10 modifications from **2c** or **1b**, respectively. Both compounds are nanomolar inhibitors of both PTR1 variants. The parent compounds, **2c** and **1b**, inhibit the parasite DHFR variants at micromolar to submicromolar levels, while **4i** is inactive against all variants of DHFR. The combination with a favorable N10 substitution is able to restore medium micromolar anti-DHFR

https://doi.org/10.1021/acs.jmedchem.2c00232
J. Med. Chem. 2022, 65, 9011−9033